

## The NSUF UCSB-1 Library ATR Irradiation Experiment

G. R. Odette – University of California, Santa Barbara – [odette@engineering.ucsb.edu](mailto:odette@engineering.ucsb.edu)

*This experiment was designed to create a new and unprecedented library of alloys and irradiation conditions to facilitate understanding of and modeling to ultimately predict and improve the behavior of structural materials used in nuclear energy systems.*

The NSUF University of California at Santa Barbara (UCSB)-1 Library Advanced Test Reactor (ATR) irradiation experiment was designed to create a new and unprecedented library of alloys and irradiation conditions to facilitate understanding of and modeling to ultimately predict and improve the behavior of structural materials used in nuclear energy systems. The UCSB-1 experiment comprised  $\approx 1400$  specimens of various types composed of 40 alloys that included tempered martensitic, nanostructured ferritic, dual phase stainless, maraging, and bainitic RPV steels. The irradiation also included Fe-Cr, Fe-Cu-Mn-Ni-Si ferritic and Cu-Nb multilayer model alloy systems. The four-cycle (145A to 146B) irradiation in the A10 position in the ATR represented 210 effective full power days. Thirty-two isothermal temperature packets contained in nine capsules were irradiated from  $\approx 1.8$  to 6.8 displacements per atom (dpa) at seven temperatures, ranging from  $\approx 320$  to  $750^\circ\text{C}$ . The side-by-side irradiation of so many alloys under so many conditions has provided a unique library that is enabling a campaign of wide ranging collaborative research studies.

### Project Description

UCSB-1 was a drop-in experiment, and so did not have thermocouples to directly monitor temperatures. Instead, a specified packet temperature was achieved by a combination of nuclear heating and a partially insulating gas gap (comprising a mixture of helium and argon). To minimize temperature uncertainties, researchers at UCSB carried out an extensive finite-element-based thermal-design study. The packets were hollow, profiled cylinders, containing multipurpose disc specimens, or cylindrical holders for other specimens. Each packet had an individual gas-gap profile designed to yield a uniform specimen centerline target temperature. Stainless steel pins provided interpacket thermal isolation and forced the heat flow to be primarily in the radial direction, crossing a minimum number of interfaces. This packet concept is illustrated in Figure 1a; the temperature-dpa profile is shown in Figure 1b. One capsule was removed from its centerline position after one reactor cycle when the contents reached a damage level of 1.8 dpa, and a replacement capsule was inserted where it remained for the rest of the irradiation. An identical packet to that irradiated at the centerline position during

the first cycle was irradiated in a lower-flux position to reach 1.8 dpa at the end of the experiment—i.e., after four cycles, providing some dpa-rate variation. The maximum damage level the experiment could reach was determined by the period of irradiation. Unfortunately, this time was limited by a reactor-power increase after the fourth cycle that would have resulted in higher temperatures. Finally, a post-irradiation adjustment of the nuclear heating rates resulted in temperature estimates being somewhat higher than planned; for example, Capsule 6 ran at  $\approx 593$  K versus the planned 563 K.

The alloys, including proper certifications, were acquired by UCSB from various sources. UCSB also fabricated all the specimens in the irradiation and loaded them into packets under the supervision of an INL quality assurance engineer. The packets were sent to INL to be loaded into capsules.

Mechanical properties of the alloys have been (or will be) variously assessed, both prior to and after irradiation by nanoindentation, microhardness, shear punch, tensile, compression, chevron wedge, and fracture toughness subsized-specimen tests. Sample specimens are shown in Figure 1c. Microstructural char-

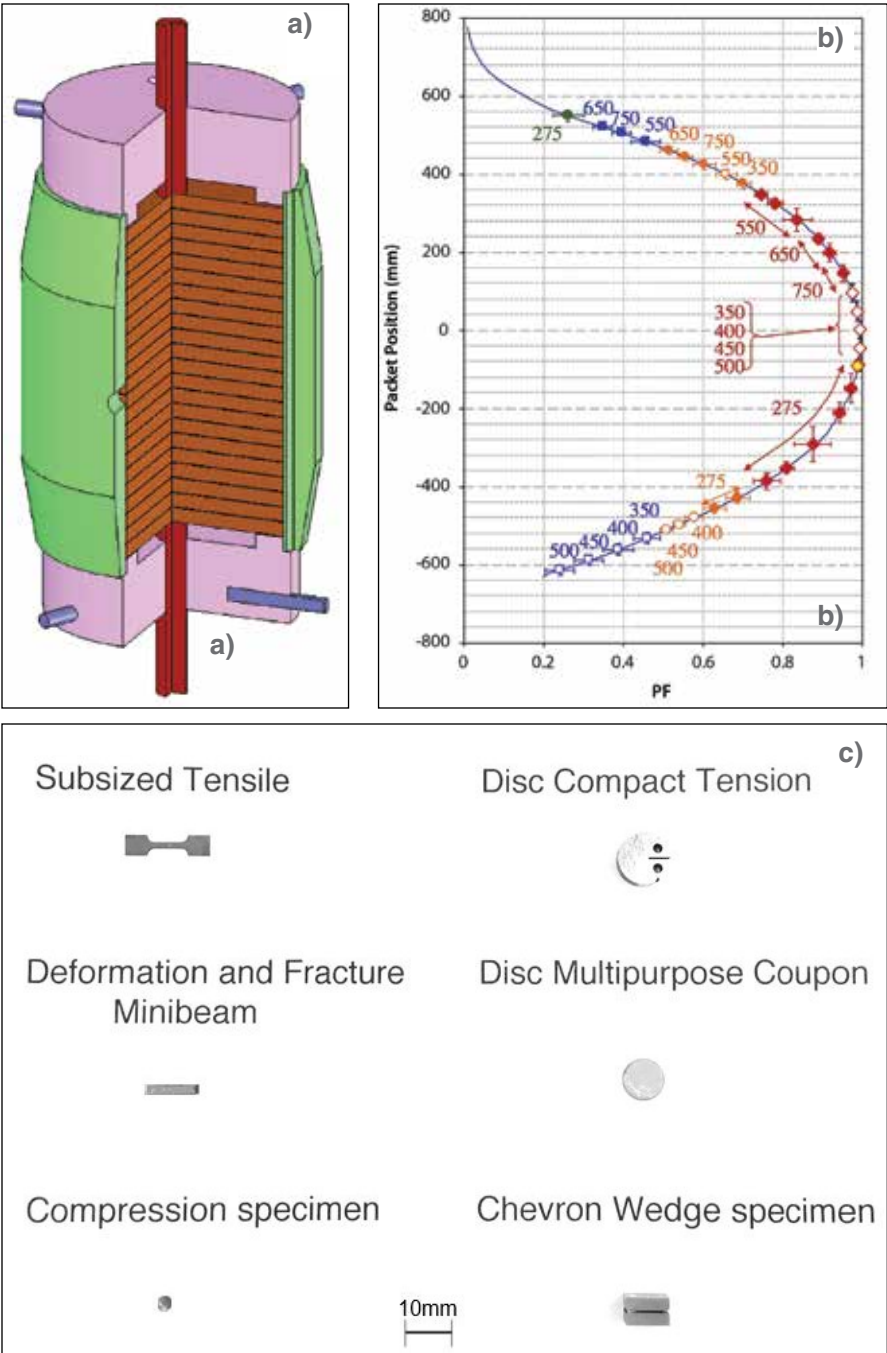


Figure 1. a) A schematic drawing of the profiled packet concept; b) the flux profile showing the packet temperatures; c) the types of specimens contained in the experiment.

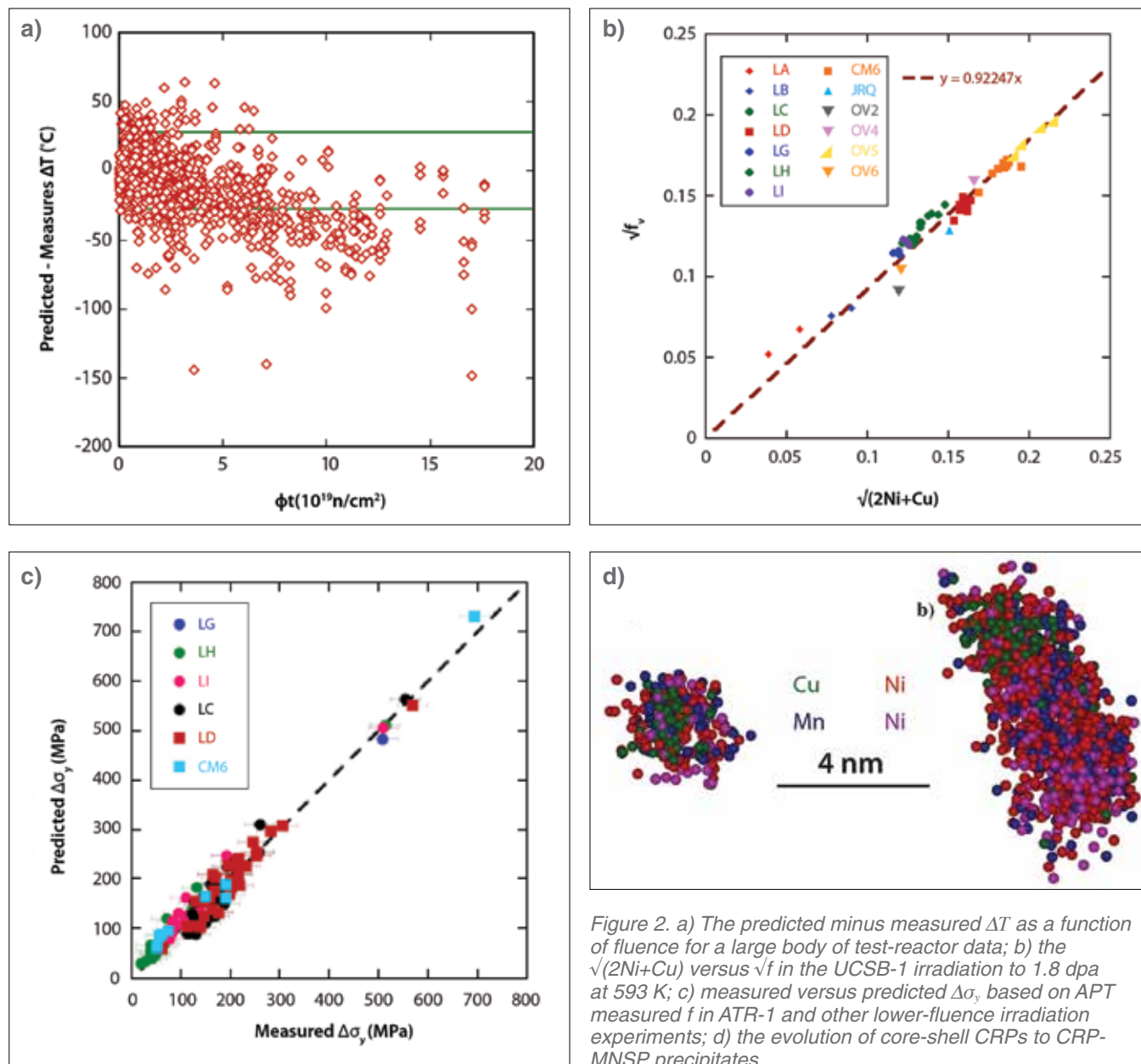


Figure 2. a) The predicted minus measured  $\Delta T$  as a function of fluence for a large body of test-reactor data; b) the  $\sqrt{(2\text{Ni} + \text{Cu})}$  versus  $\sqrt{f}$  in the UCSB-1 irradiation to 1.8 dpa at 593 K; c) measured versus predicted  $\Delta\sigma_y$ , based on APT measured  $f$  in ATR-1 and other lower-fluence irradiation experiments; d) the evolution of core-shell CRPs to CRP-MNSP precipitates.

acterization techniques available include small-angle neutron and X-ray scattering (SANS and SAXS), transmission electron microscopy (TEM), atom probe tomography (APT), and X-ray diffraction (XRD). UCSB-1 also included two lab-on-a-chip experiments, including diffusion multiples, to characterize multi-constituent alloy thermo-kinetics under irradiation, and in situ He injection assemblies to produce samples to evaluate the effects of a wide range of He/dpa ratios.

The library concept irradiation was extended to what might best be described as a “reading-club” experimental campaign. UCSB organized various collaborations around different sub-experiments, with researchers expert in different post-irradiation examination (PIE) techniques. As an example, the Fe-Cr series sub-experiment for one irradiation condition involved APT studies led by Professor Emmanuelle Marquis at the University of Michigan (UM). TEM characterization was led by Dhriti Bhattacharyya at the Australian Nuclear Science and Technology Organization (ANSTO), and irradiation hardening measurements were performed at UCSB. These data were then combined and analyzed by UCSB to develop a new microstructure-based hardening model that has been successfully extended to predict yield stress changes ( $\Delta\sigma_y$ ) in tempered martensitic structural steels. The

combination of expertise and insight provided by a reading-club approach resulted in a whole that is greater than the sum of its parts.

### Accomplishments High-fluence Embrittlement of RPV Steels

Light-water reactor pressure vessels (RPVs) are exposed to a low flux of neutrons that cause irradiation hardening and embrittlement, which manifests as a growing degradation of their fracture resistance with increasing fluence. Plant life extension of up to 80 years requires rigorous proof that the RPV maintains a very large safety margin to protect against brittle fracture under all conceivable conditions, including severe accident transients.

Embrittlement manifests as an upward shift in the temperature marking the transition from brittle cleavage to ductile fracture. RPV embrittlement is reasonably well understood and predicted up to the normal licensed plant life of 40 years; however, limited surveillance data is available for extended life, and current regulatory models underpredict accelerated test-reactor data at high fluence, as shown in Figure 2a. Current embrittlement regulations reflect the strong effect of Cu and Ni on embrittlement and are associated with the rapid formation of Cu-rich precipitates (CRPs) that harden and embrittle the steel. Theoretical models long ago predicted

a new embrittlement mechanism, associated with the formation of so-called “late blooming” Mn-Ni-Si precipitates (MNSPs), which cause severe and unexpected hardening and embrittlement at high fluence, even in nominally radiation-tolerant, Cu-free RPV steels. As studies from UCSB long ago confirmed, the MNSPs are real and highly embrittling. The multifaceted question is this: at what combination of fluences, alloy compositions, irradiation temperatures and fluxes do MNSPs form? Further, it is important to know what MNSPs are, how much of them develop, and how they relate to hardening and embrittlement?

The UCSB-1 experiment was enormously successful in addressing this challenge. Work by then Ph.D. student Peter Wells considered split melt alloys with controlled variations in Cu and Ni contents. APT and SANS showed large volume fractions ( $f$ ) of MNSPs, which are approximately independent of the alloy Cu content at the high UCSB-1 experiment fluence [1].

The MNSP  $f$  increases approximately linearly with the Ni and Cu content of the alloy

$$f \approx 0.92(2\text{Ni} + \text{Cu}),$$

consistent with the observation that MNSPs contain roughly equal fractions of Ni and Mn + Si, a result which is characteristic of the compositions of nearby G and  $\Gamma_2$  phases. These results are also consistent with CALPHAD

---

*It is important to emphasize that there are a large number of untapped opportunities remaining in the UCSB-1 library, and what has been accomplished to date can be considered just the tip of the iceberg.*

---

thermodynamic predictions [2] and with XRD measurements [3] of the composition and structure of MNSPs. As illustrated in Figure 2b, the square-root total-precipitate volume fraction ( $\sqrt{f}$ ) scales with the  $\sqrt{[2\text{Ni}(\text{MNSP}) + \text{Cu}(\text{CRP})]}$ , and the corresponding strengthening contribution scales with the  $\sqrt{f}$  in a dispersed-barrier hardening model. Figure 2c compares measured versus predicted ( $\Delta\sigma_y$ ) for a number of alloys irradiated in various experiments, including UCSB-1. Figure 2d shows that in Cu-bearing alloys, the precipitates evolve from Cu-core-Mn-Ni shell structures to Cu-appendage structures, as predicted by a recent model based on the analysis of UCSB-1 APT data [4]. The UCSB-1 data also played a key role in developing a detailed thermo-kinetic model of precipitation hardening and embrittlement in Cu-free RPV steels [5].

In summary, while the fluxes and fluences are higher than directly pertinent to extended RPV service, the UCSB-1 library provided tremendous insight on late blooming phase MNSPs. Remaining questions center on the effects of lower flux and fluence and improved predictive embrittlement models. These are being addressed in the ongoing program of studies on the UCSB-2 experiment library.

#### **Microstructural and Microstructural Evolutions in Fe-Cr Model Alloys**

Fe-8Cr to Fe-18Cr tempered martensitic and ferritic steels are the leading candidate structural alloy system for a wide range of advanced nuclear applications. While more damage resistant than fcc austenitic stainless steels, these bcc alloys experience neutron irradiation that drives complex nm-scale microstructural and microchemical evolutions that lead

to hardening and embrittlement, as well as dimensional instabilities like irradiation creep and even swelling at very high fluence. The features that develop under irradiation include dislocation loops,  $\alpha'$  (Cr-rich) precipitates, Mn, Ni, Si, Cr, P solute clusters, solute segregation, helium bubbles and, in some cases, growing voids at high fluence. Thus, one objective of developing the UCSB-1 library was to explore a number of these phenomena in a series of model Fe-3Cr to Fe-18Cr binary alloys that were irradiated side-by-side under the same conditions.

Figure 3a compares APT examinations of Fe-3Cr to Fe-18Cr binary alloys irradiated at 593 K to 1.8 dpa [6]. Precipitation of  $\alpha'$  was observed in all of the alloys containing more than 9% Cr. APT was used to fully quantify the number densities, size distributions, average radii, and mole fraction of  $\alpha'$ , and indicated nearly full  $\alpha'$  to  $\alpha$  decomposition. Both mole fraction and the matrix Cr compositions are in good agreement with the 593 K solvus boundary predicted in a recently published, first-principles guided, Fe-Cr phase diagram (which, notably, deviates substantially from earlier Cr-solubility limits based on classical CALPHAD thermodynamics). The number density and mean radius increase and decrease, respectively, with increasing Cr. These observations are consistent with classical nucleation and growth mechanisms of thermal  $\alpha'$  precipitation, that are greatly accelerated by radiation-enhanced diffusion at the low irradiation temperature.

Figure 3b shows that in the sub-saturated Fe-6Cr alloy, Si and Cr segregate, both in small clusters and visible interstitial dislocation loops [7]. The primarily Si and Cr clusters are likely

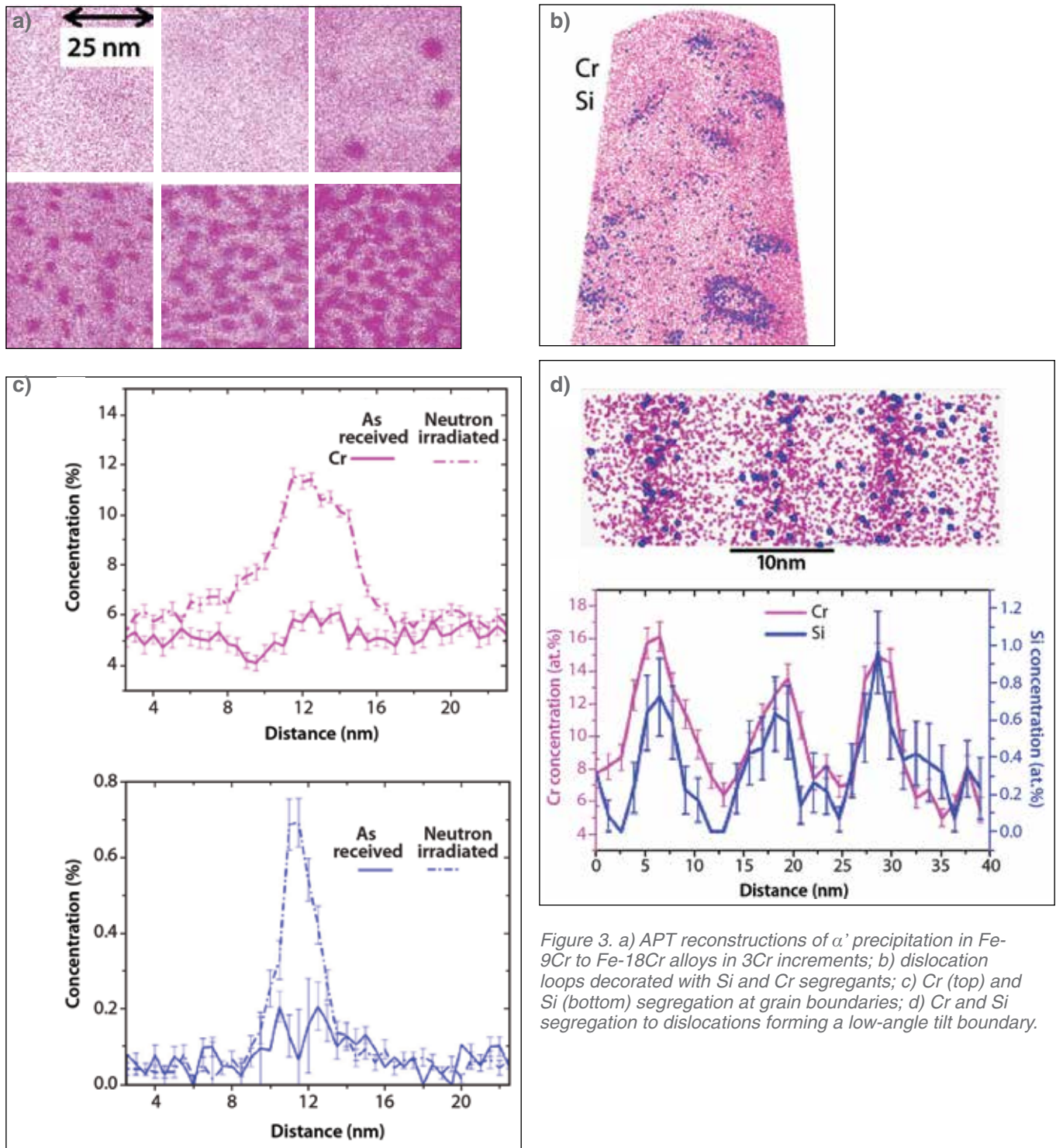


Figure 3. a) APT reconstructions of  $\alpha'$  precipitation in Fe-9Cr to Fe-18Cr alloys in 3Cr increments; b) dislocation loops decorated with Si and Cr segregants; c) Cr (top) and Si (bottom) segregation at grain boundaries; d) Cr and Si segregation to dislocations forming a low-angle tilt boundary.

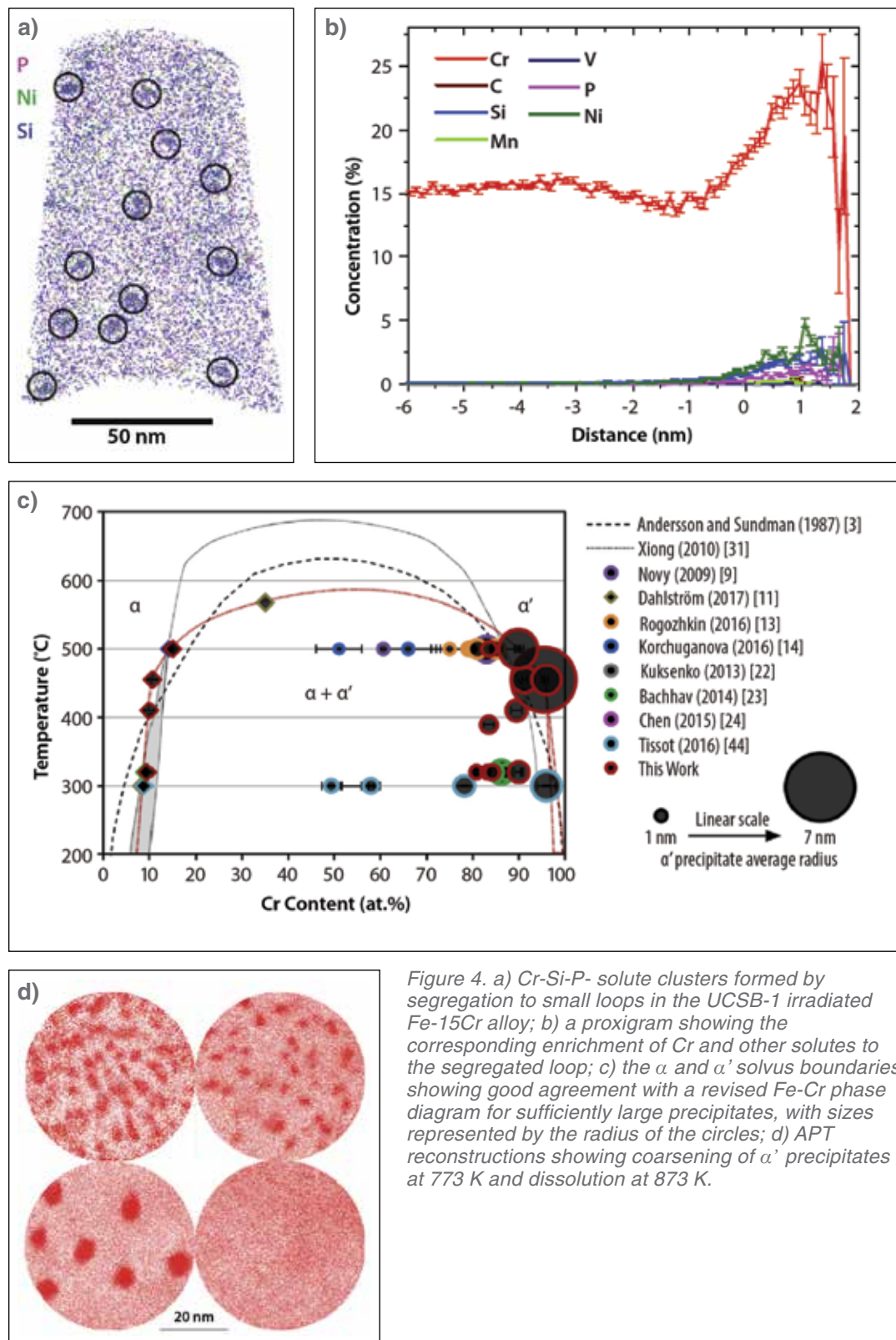


Figure 4. a) Cr-Si-P- solute clusters formed by segregation to small loops in the UCSB-1 irradiated Fe-15Cr alloy; b) a proxigram showing the corresponding enrichment of Cr and other solutes to the segregated loop; c) the  $\alpha$  and  $\alpha'$  solvus boundaries showing good agreement with a revised Fe-Cr phase diagram for sufficiently large precipitates, with sizes represented by the radius of the circles; d) APT reconstructions showing coarsening of  $\alpha'$  precipitates at 773 K and dissolution at 873 K.

associated with the smallest loops. At intermediate size, the Cr segregates to the outside of the loops while Si segregates to both the inside and outside. Both solutes segregate to the outside of the loops at larger sizes. The loops were analyzed in terms of their number density, size, habit plane and spatial distribution. Larger numbers of visible loops are observed near grain boundaries. The data from the 593 K irradiation also show segregation (enrichment) of Cr, Si (and P) at grain boundaries (Figure 3c). The C concentration is also slightly increased by irradiation, likely due to co-segregation effects with the higher Cr. Dependence of segregation on the type of grain boundary and solute enrichment at the individual dislocations were observed in low angle tilt boundaries, as demonstrated in Figure 3d.

APT studies on the Fe-15Cr alloy presented in Figure 4a show a high density of very small Cr-Si-Ni-P clusters, again likely associated with small loops [8]. These solute clusters are believed to play a critical role in irradiation hardening of Fe-9Cr tempered martensitic steels, especially at higher dpa. In addition to the expected solute clusters and  $\alpha'$  precipitates, grain-boundary Cr-carbide and nitride precipitates were also observed in Fe-15Cr alloy, which altered the local alloy chemistry. In general, less segregation of Cr at grain boundaries was observed in the 15Cr alloy, although this might be affected by nitride and carbide precipitates. Si, Ni and P generally segregate to all types of interfaces.

Examination of  $\alpha'$  precipitation over a range of irradiation temperatures and dpa, as well as following post-irradiation annealing (PIA) at both

773 and 873 K [9] has been used to establish the full Cr solvus line. Figure 4c shows that the nominal  $\alpha'$  Cr content measured by APT is generally less than predicted by the Cr-rich thermodynamic phase boundary and is a function of the  $\alpha'$  precipitate size. However, a proxigram analysis (interface-to-center concentration profile) presented in Figure 4b showed that the Cr composition at the  $\alpha'$  core approaches equilibrium values in sufficiently large precipitates, especially at higher temperatures. This demonstrates, once again, that such matrix element enrichment in precipitates is an APT artifact. Note, the  $\alpha'$  interface composition may be affected by chemistry-dependent interface energies, as well as by cascade ballistic mixing at lower temperatures. Figure 4d shows that PIA results in  $\alpha'$  coarsening at 773 K, and full  $\alpha'$  dissolution at 873 K, again consistent with the phase diagram.

These results show the effect of neutron-irradiation-enhanced diffusion on accelerating thermally driven  $\alpha'$  precipitation in Fe-Cr alloys with  $\geq 9\%$  Cr. However,  $\alpha'$  precipitation is modified in similar alloys under ion irradiation at high dpa rates. Figure 5 (top) shows  $\alpha'$  formation in an Fe-18Cr alloy following both ion and neutron irradiations at around 593 K and dose rates from  $\approx 10^{-7}$  to  $10^{-4}$  dpa/s [10]. The steady-state Cr content of the  $\alpha'$  depends on the ion irradiation dose and dose rate, confirming the contribution of ballistic mixing to diluting non-equilibrium  $\alpha'$  precipitates at high dpa rates.

These APT data were used to guide the development and calibration of a model on the effects of the

irradiating-particle type and dpa rate on  $\alpha'$  formation [11]. The model was based on the Cahn-Hilliard phase-field theory, which includes dpa-rate-dependent radiation-enhanced diffusion and cascade ballistic mixing to simulate  $\alpha'$  evolution under neutrons, heavy ions, and electron irradiation at 573 K. As shown in Figure 5 (bottom), the model predicts that higher dpa rates increase the number density of precipitates while decreasing their radius, volume fraction, and Cr content. Furthermore, the model predicts that  $\alpha'$  formation is completely suppressed above about  $10^{-5}$  dpa/s. In contrast to the ion and neutron irradiations, with high ballistic mixing rates associated with displacement cascades, electron irradiation with weak mixing had little effect on  $\alpha'$  formation up to  $10^{-3}$  dpa/s. These results show that both cascade mixing and radiation-enhanced diffusion must be accounted for, along with many other confounding factors, when attempting to emulate neutron-irradiation effects using accelerated cascade-inducing ion irradiations.

#### Neutron Irradiation Effects on The Constitutive Properties of Fe-Cr Ferritic Martensitic Steels and Fe-Cr Model Alloys: Property-Property-Microstructure Relations

True stress-true strain constitutive relations,  $\sigma(\epsilon)$ , are the most important mechanical property used in engineering analysis and design, as a required input to finite-element calculations. The UCSB-1 irradiation included sub-sized tensile specimens for a variety of ferritic-martensitic and several other steels. The test results for subset of six of these alloys, five

9Cr to 12Cr tempered martensitic steels and one 14Cr oxide-dispersion-strengthened nanostructured ferritic alloy, are shown in Figure 6 [12]. Engineering stress-strain  $s(\epsilon)$  curves for tests at 298 and 573 K were analyzed using a finite-element-based inverse method developed to derive the corresponding  $\sigma(\epsilon)$  curves, both before and after irradiation. Increases in yield stress ( $\Delta\sigma_y$ ) and reductions in uniform strain ductility ( $\Delta\epsilon_u$ ) were observed in all cases. The effect of irradiation on  $\epsilon_u$  can be understood in terms of the flow instability condition  $d\sigma(\epsilon_u)/d\epsilon = \sigma(\epsilon_u)$ . The irradiated  $\sigma(\epsilon)$  curves fall into three categories of post-yield behavior: initial strain softening, followed by perfectly plastic, nearly perfectly plastic, and reduced or unaffected strain hardening. The irradiation-induced increases in the average plastic flow stress in the range of 0 to 10% strain,  $\Delta\sigma_f$ , is generally smaller than the corresponding  $\Delta\sigma_y$  due to the reduction in strain hardening. The tensile data were also analyzed to establish relations between  $\Delta\sigma_y$  and corresponding changes in the ultimate stress,  $\Delta\sigma_u$ , as well as the effects of both test temperature and the unirradiated yield stress ( $\sigma_{yu}$ ). The latter shows that higher  $\sigma_{yu}$  correlates with lower  $\Delta\sigma_y$ , due to quadratic dispersed-barrier strengthening superposition effects.

In five out of six cases, the effects of irradiation are generally consistent with previous results on these types of alloys. However, the particular heat of the 12Cr HT-9 tempered martensitic steel in this study has a much higher irradiated strain-hardening rate and  $\epsilon_u$  than observed in earlier heats. This difference is

likely due to the correspondingly high strain-hardening rate in the unirradiated condition. The  $\epsilon_u$  in the 14Cr oxide-dispersion-strengthened nanostructured ferritic alloy was even less affected by irradiation, and the strain-hardening rate was remarkably unchanged. Again, this is likely due to the high rate of strain hardening in both conditions, primarily due to the very fine-grained microstructure, which promotes the formation of geometrically necessary dislocations.

The use of accelerated charged-particle irradiations as a surrogate for neutron irradiation, while potentially advantageous, is not without challenges. One significant challenge is extracting  $\Delta\sigma_y$  [or more generally,  $\sigma(\epsilon)$ ] data from ion-implantation depths of only a few  $\mu\text{m}$ . In principle, this type of analysis can be done using nano-indentation (NI) methods. However, it is critical that techniques to transfer NI to bulk  $\sigma(\epsilon)$  be developed and validated. To this end, small disc specimens punched from the end tabs of the tensile specimens of the same six samples considered in Figure 6, plus two additional UCSB-1 library irradiated steels, were subjected to NI measurements [13] to develop correlations between NI at various depths, and the bulk-irradiated steels tensile properties. The NI and tensile data were analyzed with various property-property correlation models. As shown in Figure 7a, a reasonably good correlation was found between high-load Berkovich microhardness ( $H_u$ , somewhat akin to Vickers microhardness) and two measures of NI hardness taken at a sufficient penetration depth

to avoid size effects. Unfortunately, the correlation between NI hardness and tensile properties was more scattered and the corresponding  $\Delta\sigma_y$  were not well predicted by the NI measurements. These results underscore the caution required in interpreting NI data and demonstrate that additional research is needed to develop better property-property correlations.

The microstructure and mechanical behavior of the Fe-6Cr in the unirradiated, self-ion-irradiated and neutron-irradiated conditions were measured and compared [14]. Ion irradiations were performed to the same dpa ( $\approx 1.8$ ) and similar temperatures, but at much higher dpa rates. The mechanical property characterization involved both NI and micro-cantilever bend tests for a wide range of beam dimensions to study the interrelationships between irradiation hardening and plasticity size effects. TEM found dislocation loop densities about  $3 \times 10^{22}/\text{m}^3$  for the neutron-irradiated condition versus only  $1.4 \times 10^{22}/\text{m}^3$  for the ion-irradiated alloy, although these differences are within typical scatter. Notably, Cr segregation to loops was only found for the neutron-irradiated case. The NI hardness increase due to neutron irradiation was about  $\approx 3$  GPa, which is roughly similar to an estimate of  $\approx 2.6$  GPa, based on Vickers microhardness data. The corresponding ion-irradiation hardening was much less, at about 1 GPa. The large difference was judged to be only partly due to the effects of dpa rate and corresponding microstructural differences.

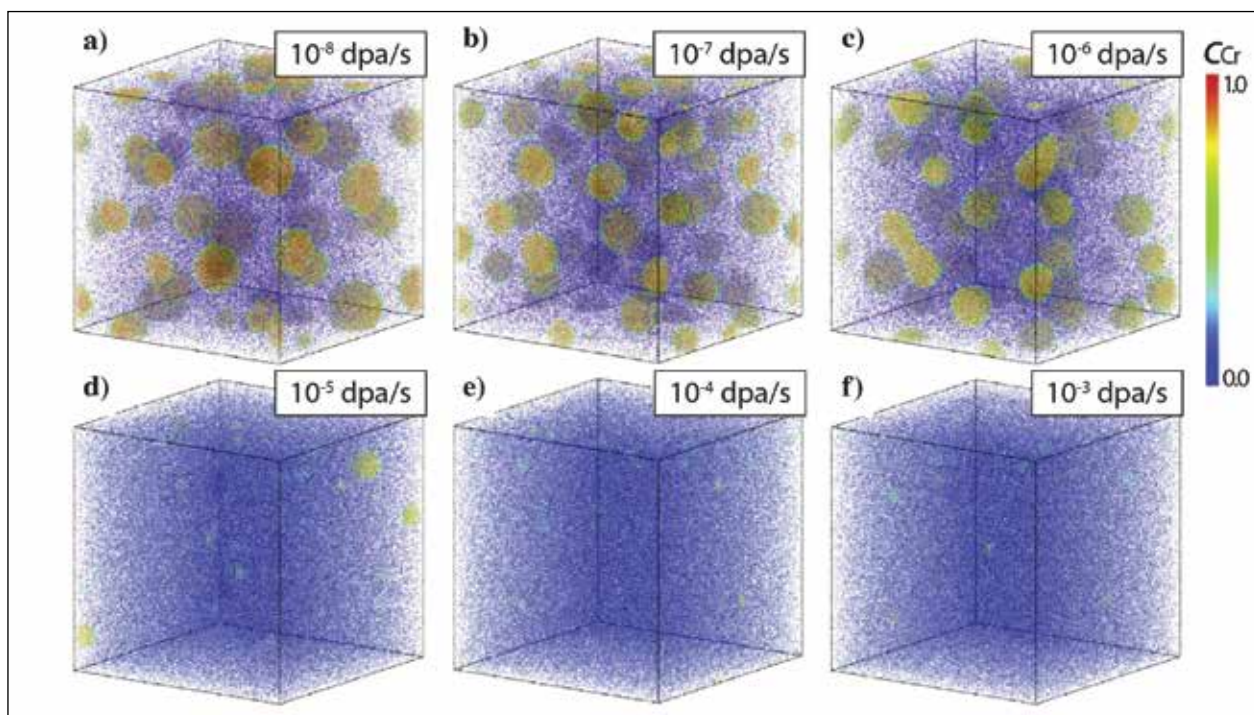
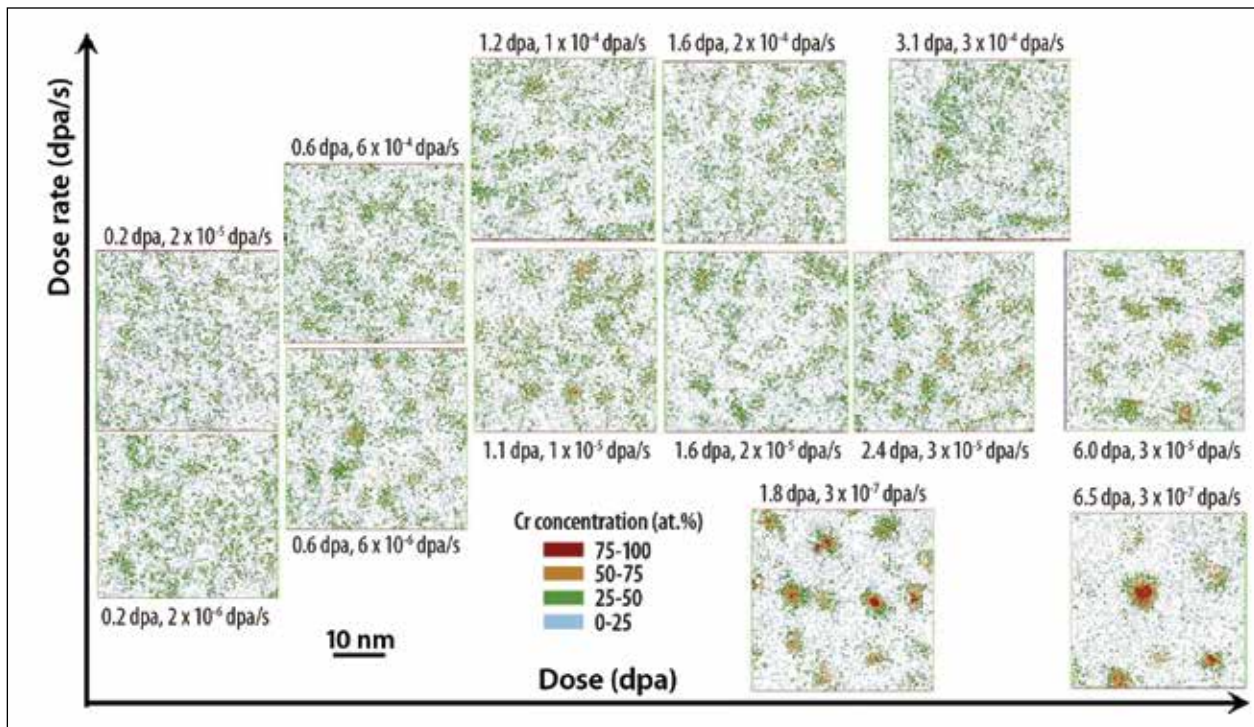


Figure 5. Top, the effect of dpa and dpa rate on precipitation in the Fe-18Cr alloy at 593 K; bottom, a model predicting the effect of dpa rate on the precipitation in a Fe-15Cr alloy at 573 K.

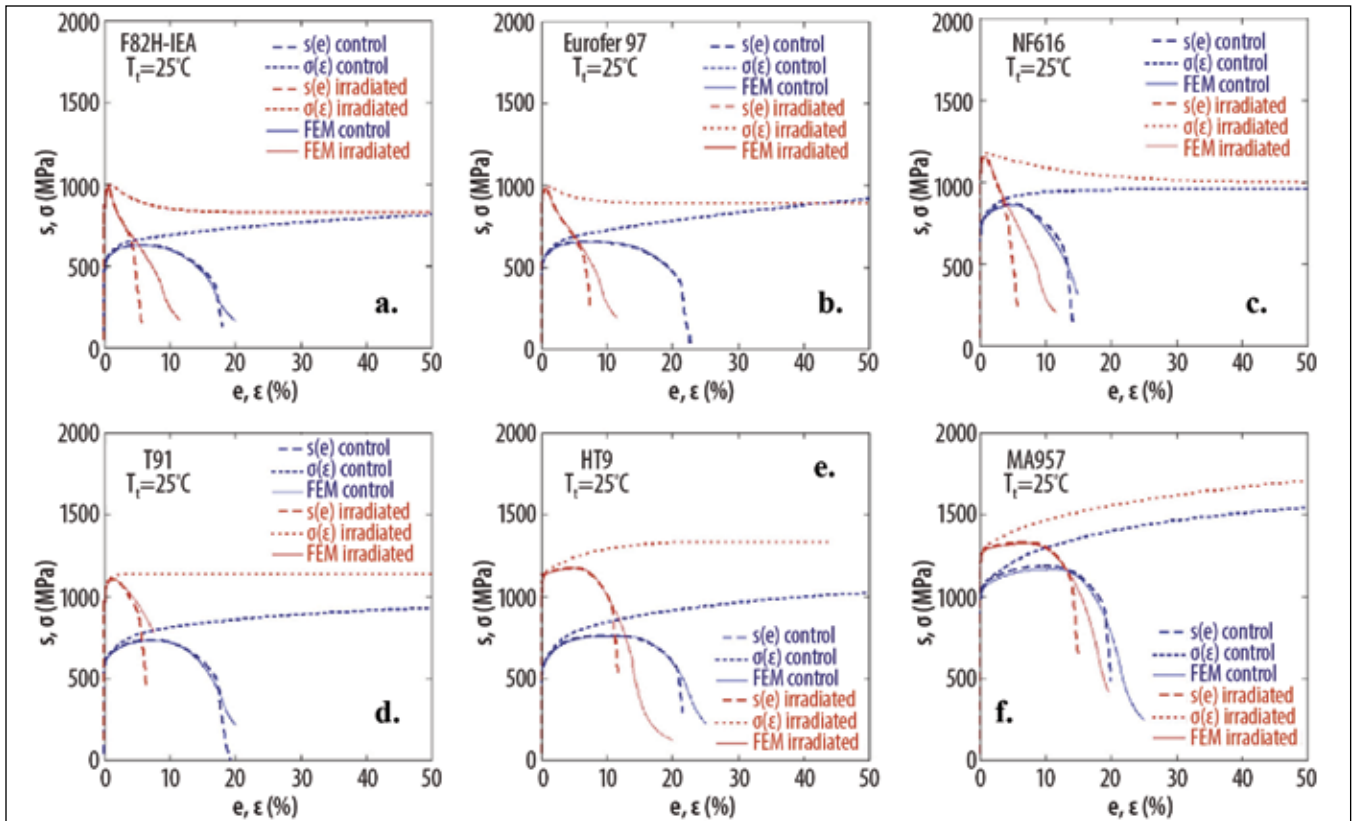
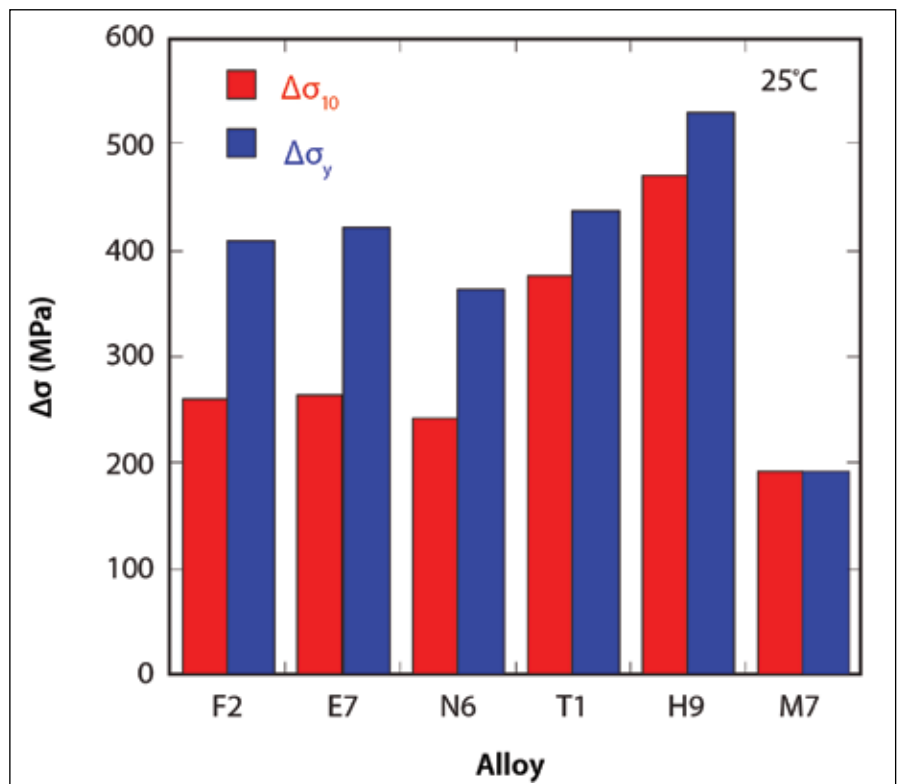
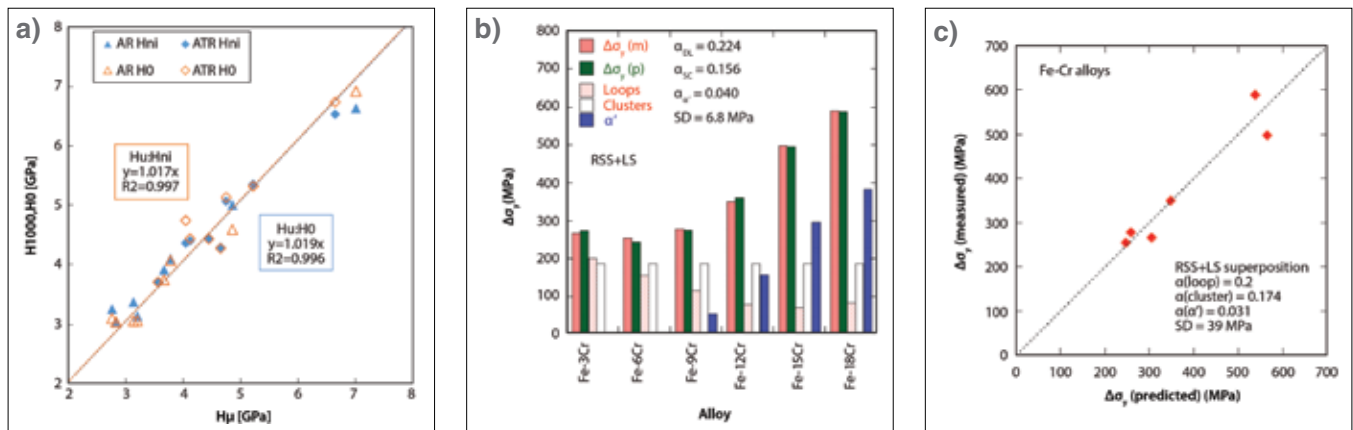


Figure 6. Top, room-temperature engineering  $s(e)$  and true-stress-strain  $\sigma(\epsilon)$  curves for six alloys in unirradiated and UCSB-1 irradiated materials 6.5 dpa at  $\sim 593$  K; bottom, the corresponding increases in the yield and flow stresses.





TEM has been used to characterize dislocation loops in the Fe-3Cr to Fe-18Cr alloys irradiated at 593 K to about 1.8 dpa [15] to estimate the obstacle strength factors ( $\alpha_i$ ) for loops, solute clusters and  $\alpha'$  precipitates. This study involved analyzing the combined microstructural and  $\Delta\sigma_y$  measurements (based on Vickers microhardness,  $\Delta H_v$ ) by least-square fitting the dispersed barrier strength factors  $\alpha_i$  and an independently derived strength superposition model. As shown in Figures 7b and c, the optimized hardening predictions are in good agreement with experiment, within expected uncertainties. Sequential 168 h isochronal anneals of the Fe-6Cr alloy from 573 to 673 K, in 25 K increments, coarsened the loop size distribution by a factor of three, and decreased the number density by a factor of 8. TEM also showed that isothermal 300 h anneals at 773 and 873 K, coarsened and dissolved the precipitates, respectively, qualitatively consistent with APT observations [9]. Coarsening was shown to be consistent with bulk diffusion controlled kinetics (aka Ostwald Ripening).

Nanostructured Ferritic Alloys (NFA) Nanostructured ferritic alloys (NFA) are Fe-12Cr to Fe-18Cr ferritic stainless steels, which are dispersion strengthened by an ultrahigh density of Y-Ti-O nano-oxide precipitates. These materials have both remarkable high-temperature strength and irradiation tolerance. As shown in Figure 8, advanced TEM (through focal series, exit wave and STEM diffraction) techniques demonstrate that large- and medium-sized oxide nanoparticles produce all the expected extra spots in the fast Fourier transformation averaged power spectra for the fcc pyrochlore  $Y_2Ti_2O_7$  complex oxide [16]. Figure 8c shows the corresponding spot pattern for the matrix without the oxide particles. Figure 8d and e show that the spot patterns for larger selected areas containing populations of much smaller oxide nanoparticles are the same in both as-fabricated and UCSB-2 library irradiated MA957. While the extra spots are blurred or streaked, and all are not visible, these patterns are also consistent with the presence of  $Y_2Ti_2O_7$ . Figure 8e shows similar spot patterns in another unirradiated NFA.

Figure 7. a) the correlation between high load and two measures of NI hardness using a Berkovich indenter; b) a bar graph showing the predicted and measured  $\Delta\sigma_y$  for the optimized dispersed barrier model for the fitted indicated strengthening factors for loops, solute clusters and  $\alpha'$  precipitates, along with their individual contributions; c) a scatter plot of the predicted versus measured  $\Delta\sigma_y$ .

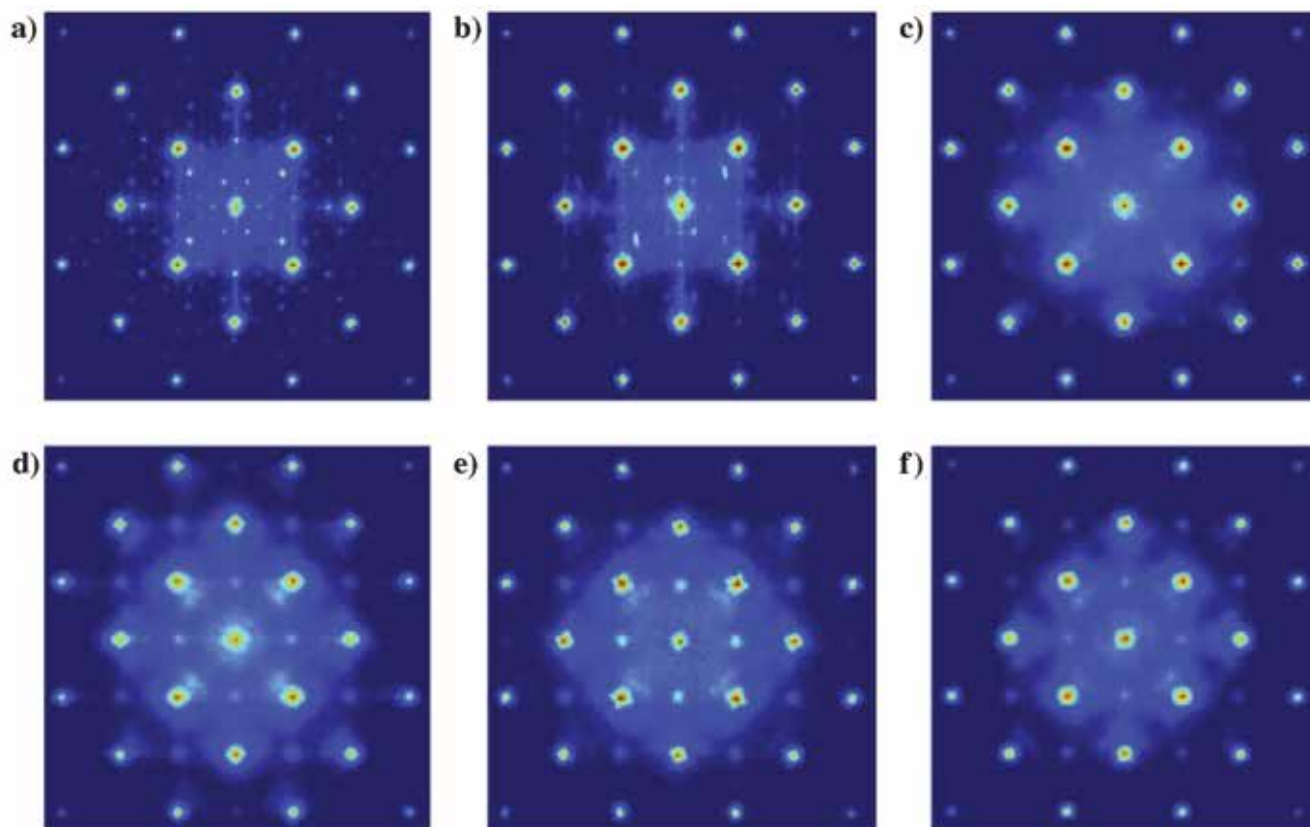


Figure 8. Fast Fourier transformation power spectra patterns for the oxide nanoparticles in indicating the presence of  $Y_2Ti_2O_7$ . Figure 8e is for MA957 following irradiation in the UCSB-2 experiment.

### Future Activities

A number of additional papers have been submitted or are nearly ready for submission, while a significant amount of post-irradiation examination and research is ongoing utilizing UCSB-1 library material in collaboration with Oxford (Roberts), UM (Marquis), LANL (Maloy), UC Berkeley (Hosemann). It is important to emphasize that there are a large number of untapped opportunities remaining in the UCSB-1 library, and what has been accomplished to date can be considered just the tip of the iceberg.

### Publications

[1.] PB Wells, T Yamamoto, B Miller, T Milot, J Cole, Y Wu and GR Odette, Evolution of manganese-nickel-silicon-dominated phases in highly irradiated reactor pressure vessel steels, *Acta Materialia* 80 (2014) 205-219 (40)

[2.] W Xiong, HB Ke, R Krishnamurthi, P Wells, L Barnard, GR Odette and D Morgan, Thermodynamic models of low-temperature Mn-Ni-Si precipitation in reactor pressure vessel steels, *MRS Communications* 4-3 (2014) 101-105 (10)

[3.] DJ Sprouster, J Sinsheimer, E Dooryhee, SK Gosh P Wells, T Stan, GR Odette and L Ecker, Structural characterization of nanoscale intermetallic precipitates in highly neutron irradiated reactor pressure vessel steels, *Scripta Materialia* 113 (2016) 18-22 (14)

[4.] S Shu, PB Wells, N Almirall, GR Odette, and DD Morgan, Thermodynamics and kinetics of core-shell versus appendage co-precip-

itation morphologies: An example in the Fe-Cu-Mn-Ni-Si system, *Acta Materialia* 157 (2018) 298-306. (0)

- [5.] H Ke, P Wells, PD Edmondson, N Almirall, L Barnard, GR Odette and D. Morgan, Thermodynamic and kinetic modeling of Mn-Ni-Si precipitates on low-Cu reactor pressure vessel steels, *Acta Materialia* 138 (2017) 10-26 (8)
- [6.] M Bachhav, GR Odette and EA Marquis, Alpha prime precipitation in neutron-irradiated Fe-Cr alloys, *Scripta Materialia* 74 (2014) 48-51 (49)
- [7.] M Bachhav, L Yao, GR Odette and EA Marquis, Microstructural changes in a neutron-irradiated Fe-6at%Cr alloy, *Journal of Nuclear Materials* 453 1-3 (2014) 334-339 (14)
- [8.] M Bachhav, GR Odette and EA Marquis, Microstructural changes in a neutron-irradiated Fe-15at%Cr alloy, *Journal of Nuclear Materials* 454 1-3 (2014) 381-386 (14)
- [9.] ER Reese, M Bachhav, PB Wells, T Yamamoto, GR Odette, EA Marquis, On  $\alpha'$  precipitate composition in thermally annealed and neutron-irradiated Fe-9-18Cr alloys, *Journal of Nuclear Materials* 500 (2018) 192-198. (2)
- [10.] ER Reese, N Almirall, T Yamamoto, S Tumey, GR Odette, EA Marquis, Dose rate dependence of Cr precipitation in an ion-irradiated Fe 18Cr alloy”, *Scripta Materialia* 146 (2018) 213-217. (2)
- [11.] JH Ke, ER Reese, EA Marquis, GR Odette, DD Morgan. Flux effects in precipitation under irradiation – Simulation of Fe-Cr alloys, *Acta Materialia* 164 (2019) 586-601(0)
- [12.] SA Maloy, TA Saleh, O Anderoglu, TJ Romero, GR Odette et al., Characterization and comparative analysis of the tensile properties of five tempered martensitic steels and an oxide dispersion strengthened ferritic alloy irradiated at approximate to 295 degrees C to approximate to 6.5 dpa, *Journal of Nuclear Materials* 468 (2016) 232-239 (7)\*
- [13.] DL Krumwiede, T Yamamoto, TA Saleh, SA Maloy, GR Odette, P. Hosemann, Direct comparison of nanoindentation and tensile test results on reactor- irradiated materials, *Journal of Nuclear Materials* 504 (2018) 135-143. (2)
- [14.] CD Hardie, GR Odette, Y. Wu, S. Akhmadaliev, SG Roberts, Mechanical properties and plasticity size effect of Fe-6% Cr irradiated by Fe ions and by neutrons, *Journal of Nuclear Materials* 482 (2016) 236-247 (2)
- [15.] D Bhattacharyya, T Yamamoto, P Wells, E Marquis, M Bachhav, Y Wu, J Davis, A Xu, GR Odette, Microstructural changes and their effect on hardening in neutron irradiated Fe-Cr alloys, *Journal of Nuclear Materials* (2019) accepted
- [16.] Y Wu, J Ciston, S Kraemer, et al, The crystal structure, orientation, relationships and interfaces of the nanoscale oxides in nanostructured ferritic alloys, *Acta Materialia* 111 (2016) 108-115 (19)

### Distributed Partnership at a Glance

NSUF and Partners	Facilities and Capabilities
Idaho National Laboratory	Advanced Test Reactor (ATR)
Collaborators	
Australian Nuclear Science and Technology Organisation	Dhriti Bhattacharyya (collaborator)
Brookhaven National Laboratory	D. J. Sprouster (collaborator), Lynne Ecker (collaborator)
Idaho National Laboratory	Jim Cole (principal investigator)
Los Alamos National Laboratory	Stuart Maloy (collaborator)
University of California, Santa Barbara	G. R. Odette (principal investigator), Nathan Almirall (collaborator), Peter Wells (collaborator), Takuya Yamamoto (collaborator)
University of Michigan	Emmanuelle Marquis (collaborator)
University of Wisconsin	Dane Morgan (collaborator)